Chemical Science

Accepted Manuscript

This article can be cited before page numbers have been issued, to do this please use: Y. Du, J. Zhang, H. Luo, Y. Zhang, Z. Liu, X. Zhang and T. Ouyang, *Chem. Sci.*, 2026, DOI: 10.1039/D5SC09305H.

ROYAL SOCIETY OF CHEMISTRY

rsc.li/chemical-science

View Article Online
DOI: 10.1039/D5SC09305H

ARTICLE

Ag-triggered Co^{4+} active sites enable OH* nucleophilic attack for efficient electrocatalytic alcohols to acids

Received 00th January 20xx,
Accepted 00th January 20xx

DOI: 10.1039/x0xx00000x

Yu-Wei Du, Jian-Yu Zhang, Hao-Jun Luo, You Zhang, Xi-Ting Zhang, Ting Ouyang* and Zhao-Qing Liu*

Selective oxidation of primary alcohols to carboxylic acids is widely employed transformation in organic chemistry. However, the intrinsic mechanism by which R(Ph)–OH (R is an alkyl or phenyl) in alcohols undergoes dehydrogenation to form oxygen-rich acids remains elusive. Here, we demonstrate an efficient interface cooperative structure ($Ag/Co(OH)_2$) as electrocatalyst. $Ag/Co(OH)_2$ significantly lowers the energy barrier of the rate-determining step (Ph-CHO* + OH* → Ph-$CH(OH)_2$*) to 0.78 eV and enhances the chemisorption of Ph-CHO* intermediates to -0.89 eV, both superior to $Co(OH)_2$ (ΔG = 1.22 eV, G_{ads} = -0.72 eV), with the Faraday efficiency of carboxylic acids reached 99.6% under mild conditions. Kinetic studies reveal the formation of Co^{4+}-O species on the composite surface, promoting the capture of OH*. Furthermore, $Ag/Co(OH)_2$ also demonstrates excellent Faradaic efficiency (ranging from 41.48% to 88.73%) in the oxidation of methanol, furfuryl alcohol, ethylene glycol, and 5-hydroxymethylfurfural to their corresponding carboxylic acids. This work provides a new idea for designing efficient and stable electrocatalytic carboxylic acid synthesis catalysts.

Introduction

As the problems of fossil fuel depletion and environmental degradation intensify, green and friendly hydrogen energy has received much attention due to its sustainability and low environmental load characteristics.[1,2] Driven by renewable electricity, water electrolysis technology is expected to be an ideal long-term low-carbon method for hydrogen production.[3,4] However, the overpotential of the anodic oxygen evolution reaction (OER) is relatively high, which limits the hydrogen production efficiency of the overall water electrolysis process. Therefore, it is urgent to develop alternative reaction systems with lower overpotential.[5-8]

The catalytic oxidation of primary alcohols or primary aldehydes to carboxylic acids is one of the most important chemical transformations and widely used in fine chemicals production.[9] Currently, the industrial oxidation process still faces the challenge of thermal management under high-temperature and high-pressure conditions. If the reaction heat cannot be effectively removed, it is likely to cause local overheating, leading to catalyst deactivation, reduced selectivity, and even safety issues such as "runaway reaction". The traditional Cr/Mn-based compounds and bromide catalysts not only possess toxicity, but also have high costs for recovery and disposal, which seriously hinders the development of green chemical processes. From the perspectives of thermodynamics and kinetics, the electro-oxidation reactions of primary alcohols or primary aldehydes can be carried out at a potential lower than that of the OER.[10,11] Therefore, achieving the electro-catalytic conversion of alcohols to carboxylic acids under mild conditions not only provides a feasible path for replacing the high overpotential OER, but also can be coupled with renewable energy sources. At the anode, high value-added chemicals can be simultaneously produced, achieving efficient conversion of electrical energy to chemical energy.[12-15] The electrocatalytic alcohol oxidation reaction is designed with multiple electrochemical steps (proton coupling - charge transfer (PCET)) and electrochemical steps (C-C cleavage).[16,17] Through different reaction pathways, various products can be obtained. Furthermore, the electronic structure and steric hindrance of different alcohol molecules (such as aromatic alcohols and aliphatic alcohols) also affect the catalytic rate.[18] Accordingly, developing efficient catalyst to regulate the oxidation process of various alcohols and obtain the desired high-value chemicals still remains a significant challenge.

$Co(OH)_2$, as a highly promising anode catalyst, is rich in surface hydroxyl groups that can dehydrogenate from Co^{2+}-OH to form Co^{3+}-O species, acting as a proton mediator to efficiently drive the PCET process during the alcohol oxidation.[19-22] Furthermore, the Co^{3+}-oxo species over CoOOH formed after the reconstruction of $Co(OH)_2$ play a key role in the benzyl alcohol oxidation reaction (AOR, using BA as the substrate) process.[23-25] However, $Co(OH)_2$ has a limited range to regulate the adsorption strength of the intermediates, which can easily lead to desorption or over-oxidation of the reacting intermediates. In this process, the adsorption behavior of the reacting molecules with catalyst directly affects the electrooxidation efficiency. Notably, constructing active metal coupled transition metal compound supporter is an effective strategy to enhance the electrocatalytic activity.[26,27] The

School of Chemistry and Chemical Engineering/Institute of Clean Energy and Materials/Key Laboratory for Clean Energy and Materials/Huangpu Hydrogen Innovation Center, Guangzhou University, Guangzhou 510006, P. R. China.

† Supplementary Information available: [details of any supplementary information available should be included here]. See DOI: 10.1039/x0xx00000x

View Article Online
DOI: 10.1039/D5SC09305H

ARTICLE

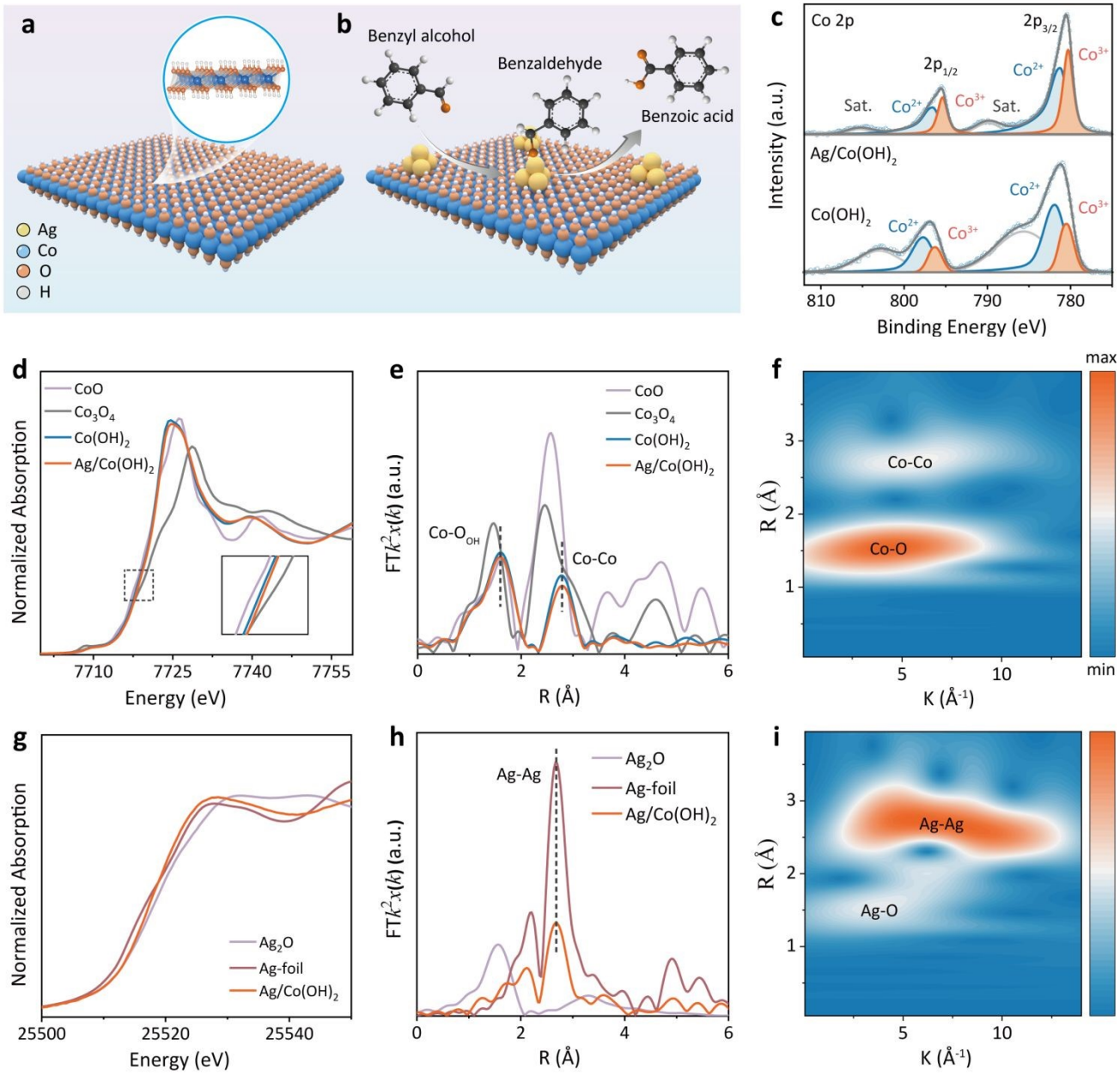

Figure 1. (a) Diagram of $Co(OH)_2$. (b) Schematic diagram of the electro-oxidation of BA on the surface of $Ag/Co(OH)_2$. (c) Co 2p XPS spectrum. (d) Co K-edge XANES spectra and (e) the corresponding EXAFS spectra. (f) The contour map of Co K-edge WT-EXAFS. (g) Ag K-edge XANES spectra and (h) the corresponding EXAFS spectra. (i) The contour map of Ag K-edge WT-EXAFS. (To avoid the analytical effects of nickel foam on cobalt, the catalyst was grown on carbon cloth for XRD, XANES and FT-EXAFS measurements).

construction of such heterogeneous interfaces not only enhances the electrical conductivity,[28] but also optimizes the local coordination environment of the active sites and regulates the adsorption behavior,[29-31] thus significantly improving the catalytic performance. Recently, the nano-Ru-modified $Ni(OH)_2$ enhanced the adsorption capacity of phenol by regulating the electronic structure of Ru sites, thereby achieving its efficient conversion into p-quinone.[32] By utilizing the thermal and

View Article Online
DOI: 10.1039/D5SC09305H

electronic plasmonic effects of Ag, Ag-modifying CoV-LDH@G with Mott-Schottky heterojunction significantly improved the OER performance.[33] In addition, Pd-Cu_2O nanoparticle with the enhanced adsorption of CO intermediates, achieved a significant improvement in methanol oxidation reaction (MOR) activity.[34] Certainly, it is crucial to enhance the catalytic performance of catalytic oxidation of alcohols by rationally modulating the adsorption energy of key reaction intermediates on the catalyst surface.

In this work, we demonstrate a simpe and feasible electrocatalytic strategy for the oxidation of primary alcohols over silver-modified cobalt hydroxide ($Ag/Co(OH)_2$) electrocatalyst. AOR was selected as a model reaction to evaluate the catalytic performance. A series of electrochemical tests in alkaline solution revealed that the $Ag/Co(OH)_2$ exhibits high activity for the AOR, with high selectivity for the generation of benzoic acid (BAC) products (Figure 1a-b). Among them, the Faraday efficiency (FE) of BAC reaches 99.9% at a potential of 1.45 V *vs.* RHE. The experimental characterization and theoretical calculations show that the silver modification could effectively modulate the surface charge transfer kinetics of the catalyst and induce the formation of high valence active sites (Co^{4+}-O). More importantly, $Ag/Co(OH)_2$ exhibits superior performance over $Co(OH)_2$ in both the activation barrier of the rate-limiting step of the oxidation reaction (the combination of Ph-CHO* and OH*) (0.78 eV *vs* 1.22 eV) and the adsorption energy of Ph-CHO at the interface (-0.89 eV *vs* -0.72 eV), thereby achieving the a FE of 99.6% for Ph-COOH under mild conditions. Impressively, the unique interface cooperative mechanism of $Ag/Co(OH)_2$ can adapt to the electronic structure and spatial configuration of different alcohol molecules, and also affords universal oxidation activity for other primary alcohols (methanol, furfuryl alcohol, ethylene glycol, and 5-hydroxymethylfurfural, the corresponding FE of the acid can reach 41.48% to 88.73%).

Results and discussion

Catalyst Synthesis and Characterization. The $Ag/Co(OH)_2$ was synthesized on the nickel foam (NF) via electrodeposition and spontaneous redox methods. The scanning electron microscopy (SEM) image shows that $Co(OH)_2$ is uniformly plated on NF in a dense nanosheet morphology. With the introduction of Ag, the sample is transformed into a complex structure of nanoparticles and ultrathin nanosheets stack on top of each other (Figure S1). High-resolution transmission electron microscopy image (HRTEM) exhibits the presence of both Ag (111) and $Co(OH)_2$ (100) stripes corresponding to $Ag/Co(OH)_2$ (Figure S2). Also, XRD spectra shows crystallographic peaks consistent with Ag and $Co(OH)_2$ (PDF# 04-0783 and PDF# 51-1731) (Figure S3), indicating the successful synthesis of $Ag/Co(OH)_2$. The quantitative determination of Ag and Co in the catalyst was performed using inductively coupled plasma optical emission spectrometry (ICP-OES, Table S1). The results indicate that the content of Ag in the material is relatively low (5.19 atomic%). Energy dispersive spectroscopy (EDS) further confirms that the elements Co and O are uniformly distributed, while Ag appears as a blocky aggregation on top of Co (Figure S4). The surface composition and electronic states of $Co(OH)_2$ before and after Ag modification were examined by X-ray photoelectron spectroscopy (XPS). Compared to $Co(OH)_2$, Ag modification promotes the formation of Co^{3+} and oxygen vacancies (Figure 1c and S5).

The X-ray absorption near-edge structure (XANES) of Co is also displayed (Figure 1d and S6a). The absorption edges of the white line peaks correlate with the 1s→4p orbital leaps of the electrons, reflecting the valence state information of the catalysts. $Ag/Co(OH)_2$ and $Co(OH)_2$ show white line peaks that are higher than CoO and lower than CoOOH, which implies that the average oxidation states of the Co atoms in $Ag/Co(OH)_2$ and $Co(OH)_2$ are between +2 and +3. And the higher intensity of the white line peaks in $Ag/Co(OH)_2$ confirms that the introduction of Ag elevates the valence state of Co, which is consistent with the results of XPS. The Fourier transform extended X-ray absorption fine structure (FT-EXAFS) spectrum shows two distinct peaks at 1.6 Å and 2.8 Å, corresponding to the coordination structures of Co-O and Co-Co (Figure 1e and S6b). The corresponding EXAFS fitting images in K and R space are illustrated (Figure S7-8), and the detailed numerical values are presented (Table S2). EXAFS analysis using wavelet transform (WT) provides the same evidence (Figure 1f and S9).[35] It is noteworthy that the coordination number of Co-O decreases from 6.2 to 5.9 after Ag introduction, suggesting the formation of oxygen vacancies, which matches the results of XPS O1s (Figure S5a). In addition, Ag was also subjected to K-edge XANES measurements. The results indicate that the valence state of Ag is located between 0 and +1 valence and the main coordination structure is Ag-Ag (Figure 1g-i, S10-S12, and Table S3).

Performance Evaluation of the Alcohol Oxidation Reaction. BA was selected as a model substrate for alcohol oxidation, and the performance of the catalysts in the AOR was evaluated using cobalt-based material as the anode and platinum sheet electrode as the cathode. Linear scanning voltammetry (LSV) analysis was first performed. As shown in Figure 2a, $Ag/Co(OH)_2$ exhibits the earliest onset potential and higher current density. One of the oxidation peaks at 1.21 V *vs.* RHE was identified as the Co^{2+}/Co^{3+} oxidation peak, which was related to the oxidation of $Co(OH)_2$ to CoOOH. For $Co(OH)_2$, the oxidation peak appeared at 1.25 V *vs.* RHE, suggesting that Ag modification promotes the electrooxidation of Co^{2+}-OH to Co^{3+}-OH. Cyclic voltammetry (CV) curves exhibit the same results (Figure 2b and S13).

Within the potential range of 1.2 V - 1.6 V *vs.* RHE, the AOR current density of $Ag/Co(OH)_2$ is overall higher than that of $Co(OH)_2$ (Figure 2c), further confirming that the promoting effect of Ag modification enhances the electrocatalytic activity. In addition, the Tafel slope for different potential ranges are displayed in Figure 2d. The Tafel value of $Ag/Co(OH)_2$ (325 mV dec^{-1}) is lower than that of $Co(OH)_2$ (501 mV dec^{-1}). Combined with the electrochemical impedance spectroscopy (EIS) measured at open-circuit potentials, both indicate that the introduction of Ag could accelerates the reaction kinetics (Figure S14). In general, the double-layer capacitance (C_{dl}) is directly related

to its electrochemically active surface area (ECSA), with larger C_{dl} leading

View Article Online
DOI: 10.1039/D5SC09305H

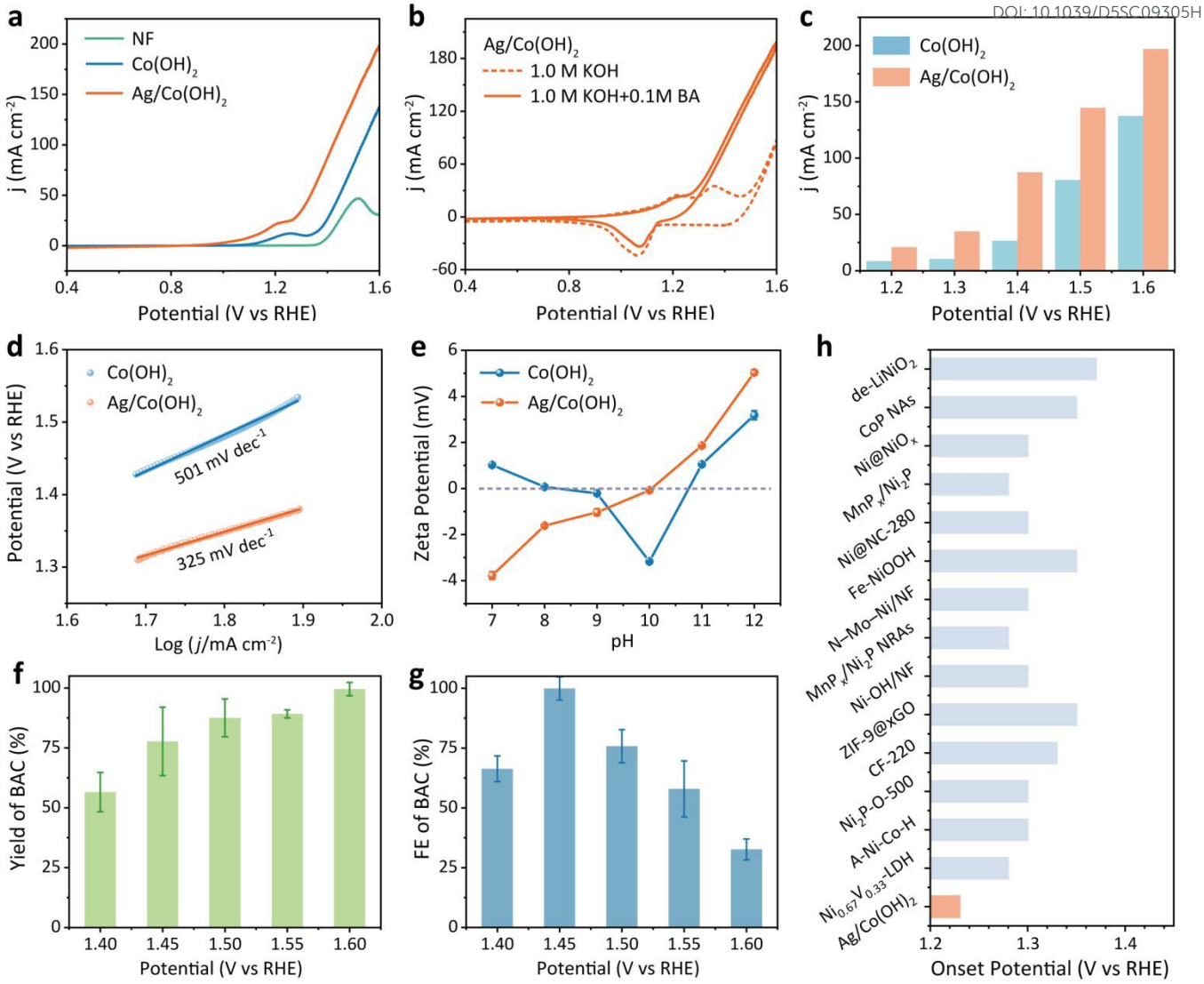

Figure 2. (a) LSV curves of Ni foam supported $Co(OH)_2$ and $Ag/Co(OH)_2$ catalysts in 1.0 M KOH + 0.1 M BA. (b) CV curves of $Ag/Co(OH)_2$ catalyst in 1.0 M KOH + 0.1 M BA (solid line) and 1.0 M KOH (dotted line) (c) Comparison of current density of $Co(OH)_2$ and $Ag/Co(OH)_2$ catalysts at different potentials. (d) Tafel slopes of $Co(OH)_2$ and $Ag/Co(OH)_2$ catalysts. (e) Zeta potential of $Co(OH)_2$ and $Ag/Co(OH)_2$ under different pH conditions. (f-g) The yield and FE of BAC at different voltages during AOR on $Ag/Co(OH)_2$. (h) Comparison of AOR onset potential of $Ag/Co(OH)_2$ catalyst with the reported state-of-the-art catalysts.

to larger ECSA. C_{dl} values of $Ag/Co(OH)_2$ are significantly higher than those of $Co(OH)_2$ (Figure S15), indicating that the introduction of silver effectively enhanced the ECSA of the material, thereby improving its catalytic performance. Moreover, the C_{dl} values of both catalysts measured in 1.0 M KOH are higher than their corresponding values in the 1.0 M KOH +0.1 M BA. This might be due to the adsorption of BA on the catalyst surface at the measurement potential, partially covering the active sites available for double-layer charging. The zeta potential reflects the potential difference between the sliding surface of a particle and a solution. This is affected by pH, as a change in pH alters the protonation state of the functional groups on a particle's surface.[36, 37] The pH at which the zeta potential is zero is the isoelectric point (IEP). In Figure 2e, the IEP of $Ag/Co(OH)_2$ (~10) increases significantly compared to $Co(OH)_2$ (~9), maintaining a more positive and stable zeta potential in the pH > 10 range.

View Article Online
DOI: 10.1039/D5SC09305H

ARTICLE

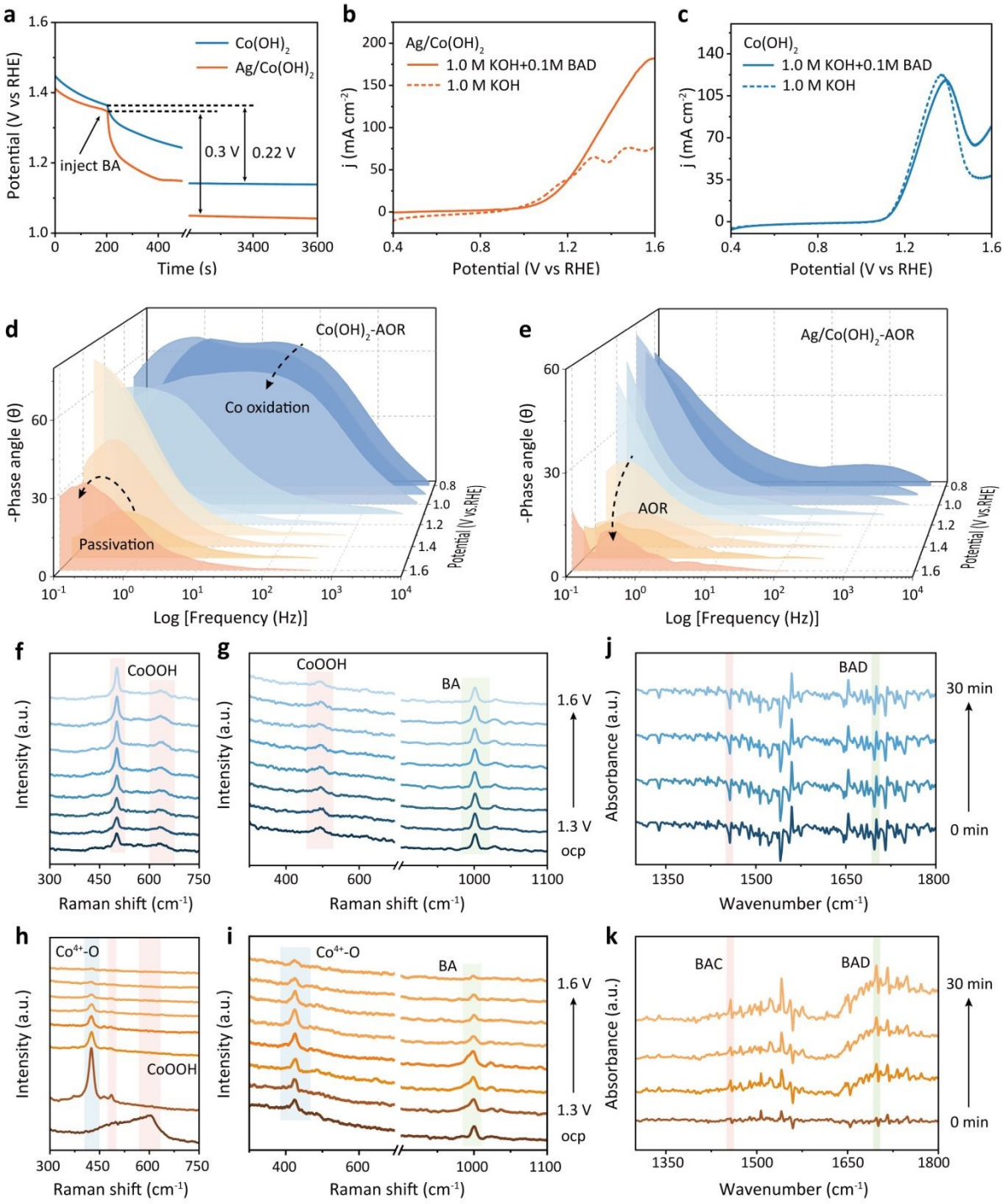

Figure 3. (a) The OCP changes of the $Co(OH)_2$ and $Ag/Co(OH)_2$ catalysts in 1.0 M KOH after 0.1 M BA injected. (b-c) LSV curves of $Ag/Co(OH)_2$ and $Co(OH)_2$ catalysts in 1.0 M KOH with or without 0.1 M BAD. (d-e) In situ impedance-phase angle of $Co(OH)_2$ and $Ag/Co(OH)_2$ during electrooxidation with at various potentials (0.8−1.6 V *vs.* RHE). In situ Raman spectra of $Co(OH)_2$ (f-g) and $Ag/Co(OH)_2$ (h-i) during OER (1.0 M KOH) and AOR (1.0 M KOH + 0.1 M BA), respectively. (j-k) In-situ FT-IR spectra of $Co(OH)_2$ and $Ag/Co(OH)_2$ during AOR.

View Article Online
DOI: 10.1039/D5SC09305H

ARTICLE

Notably, the zeta potential of $Co(OH)_2$ exhibits a non-monotonic change (positive → negative → positive) with the increase of pH, potentially due to surface remodelling under strong alkaline conditions, whereas $Ag/Co(OH)_2$ shows a monotonic positive shift. This suggests that introducing Ag enhances the stability of the hydroxyl groups on the surface of $Co(OH)_2$ in alkaline environments, and increases the positive electronegativity of the surface by optimizing the interfacial charge, thus promoting the adsorption of OH^-.

The electrocatalytic activity of $Co(OH)_2$ and $Ag/Co(OH)_2$ on AOR was investigated using a 1.0 M KOH + 0.1 M BA as electrolyte, and the post-oxidation products were detected by gas chromatography-mass spectrometry (GC-MS). The electrolyte after 12 h of reaction at 1.4 V *vs.* RHE was collected and analysed (Figure S16). Clearly, the $Co(OH)_2$-catalyzed product is present with both benzaldehyde (BAD) and BAC, while $Ag/Co(OH)_2$ is dominated by BAC, indicating that the modification of Ag might affect the desorption of intermediate products and thus achieve highly selective oxidation of BA to BAC. The modification amount of Ag in the catalyst was optimized using LSV and GC-MS data (Figure S17-18). When the concentration of Ag^+ is 13.3 mM, it affords the best AOR performance at a high potential and faster product formation (higher GC-MS peak area). In order to further quantify the reactants and products, standard curves for BA, BAD and BAC were made (Figure S19). The yield and FE of the BAC with the voltage range of 1.4 V-1.6 V *vs.* RHE are shown in Figure 2f and 2g. And the yield increases with the increase of potential, however, the FE decreases with increasing potential, the possible reason being that at higher potentials, OER competes with the AOR and the charge is dispersed. Therefore, it is necessary to select a suitable potential to minimize the effect of OER competition. 1.45 V vs. RHE is the optimal potential at which the yield of BAC reaches 77.7% and FE is 99.6%. After a 12 h AOR reaction, the structure of the $Ag/Co(OH)_2$ catalyst was characterized (Figure S20-22). The XRD results show that the intensity of the characteristic diffraction peaks of the metal Ag weakened, indicating that Ag undergo a chemical state or dispersion state transformation under electrocatalytic conditions. EDS mapping and XPS analysis confirm that the Ag element doesn't leach out and remained uniformly distributed. The intensity of the oxygen vacancy-related peak in the O 1s XPS spectrum increase significantly after the reaction, indicating a higher concentration of surface oxygen defects. These oxygen vacancies and the highly dispersed Ag species form a more efficient catalytic interface, thereby supporting the performance of $Ag/Co(OH)_2$ in maintaining a high FE during the long-term reaction. The $Ag/Co(OH)_2$ catalyst exhibits a lower onset potential compared to other reported AOR catalysts (Figure 2h and Table S4).[11, 13, 38-49]

Mechanistic Elucidation. In order to further investigate the adsorption behavior of BA on the catalyst, an open-circuit potential test was performed. In Figure 3a, the potential drop of $Ag/Co(OH)_2$ (0.30 V) is higher than that of $Co(OH)_2$ (0.22 V) with the addition of 0.1 M BA, also at 200 s, indicating that the BA better adsorbs on $Ag/Co(OH)_2$, resulting in the improved the electrocatalytic performance of catalyst. To further verify that the modification of Ag could modulate the product selectivity of AOR, the catalytic performance of the catalysts in 1.0 M KOH + 0.1 M BAD was also investigated. Compared with the oxidizing activity of $Co(OH)_2$, $Ag/Co(OH)_2$ shows better oxidizing activity for BAD (Figure 3b and 3c), which leads to further oxidation of the intermediate product. Next, the oxidation process occurring at the catalyst interface during OER and AOR were monitored and analyzed using *in-situ* EIS. For $Co(OH)_2$, the phase angle gradually decreases with increasing voltage (0.8 V-1.1 V *vs.* RHE) in the high frequency region, which is associated with the phase transition process from $Co(OH)_2$ to CoOOH inside the catalyst. When the voltage exceeds 1.4 V *vs.* RHE, the phase angle in the low-frequency region gradually decreases, corresponding to the proceeding of OER. Upon addition of BA, the phase transition in the low-frequency region was advanced to 1.3 V *vs.* RHE (Figure 3d and S23), consistent with the LSV results in Figure 2a. In Figure 3e, $Ag/Co(OH)_2$ displays a smaller phase angle at all potentials, which indicates faster reaction kinetics, i.e., faster charge transfer, at its surface. Moreover, during AOR, $Co(OH)_2$ shows a passivation signal at high potential 1.6 V *vs.* RHE, which could not occur at the $Ag/Co(OH)_2$ interface. This might be due to the slower AOR kinetics at the $Co(OH)_2$ interface compared to $Ag/Co(OH)_2$. At high oxidation potentials, such kinetic limitation promotes the accumulation of OH^+ oxide species, eventually leading to the formation of a CoOOH passivation layer.

In order to investigate the interfacial structure evolution of the catalysts during the reaction process, the *in-situ* Raman spectroscopy tests were performed (Figure 3f-i and S24). During the OER of $Ag/Co(OH)_2$ catalyst, two characteristic peaks at 484 cm^{-1} and 602 cm^{-1} are observed at the OCP, which may be attributed to the E_g and A_{1g} modes of CoOOH, respectively.[10, 35] With the increase of applied potential, a new peak at 425 cm^{-1} appears, and the signal could be clearly assigned to the characteristic vibration of CoO_2 or CoO_2-like species,[17, 20] indicating that the catalyst surface undergoes a transition from Co^{3+} to Co^{4+} oxidation state transition. Notably, when BA is introduced into the electrolyte, the intensity of Co^{4+}-related signals at 425 cm^{-1} gradually decreases with increasing potential, suggesting that the oxidation process of BA consumes Co^{4+} active species, leading to their reduction to the lower valence state. This result is further corroborated by the attenuation of the intensity of the characteristic peak of the benzene ring at 1000 cm^{-1},[50] confirming the depletion of the BA molecule in the reaction. In contrast, the Raman spectra of $Co(OH)_2$ catalysts in the same potential interval (OER and AOR systems) do not show significant changes, and their peak positions and intensities remain stable, indicating that the material could not undergo any obvious valence or phase structure

View Article Online
DOI: 10.1039/D5SC09305H

ARTICLE

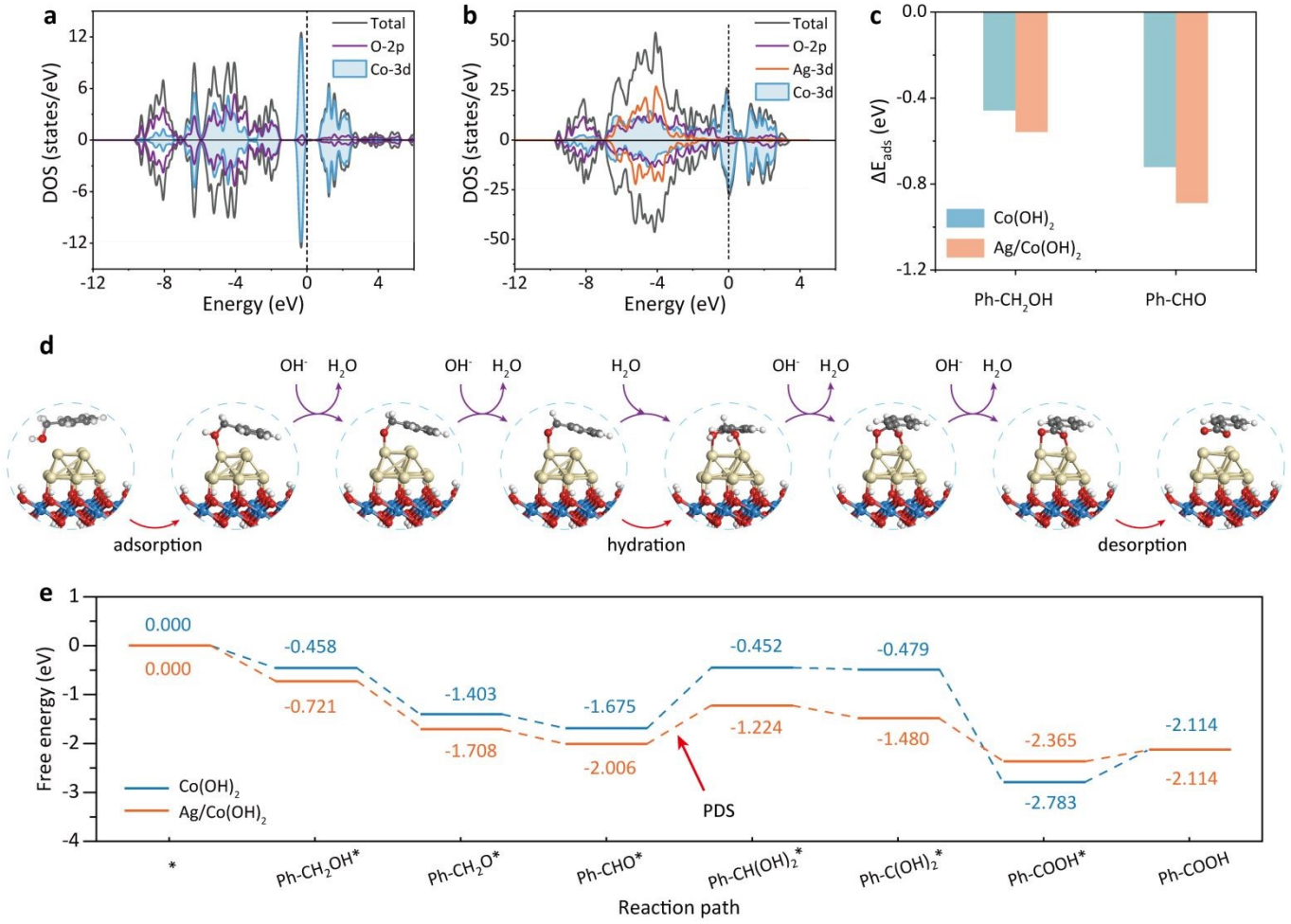

Figure 4. (a-b) The calculated density of states of (a) $Co(OH)_2$ and (b) $Ag/Co(OH)_2$ surfaces. (c) Comparison of the adsorption energy of Ph-CH_2OH (BA) and Ph-CHO (BAD) on different catalysts. (d) Adsorption configurations and (e) Gibbs free energy diagrams of BA to BAC on $Ag/Co(OH)_2$. Atoms are color-coded as follows: Co (blue), O (red), Ag (yellow), C (gray), and H (white).

transition under the reaction conditions. This result highlights the key regulatory role of Ag modification on the electronic structure and catalytic activity of $Co(OH)_2$. The adsorption behavior of the catalyst during the AOR process was investigated by *in-situ* Fourier transform infrared spectroscopy (FTIR) at a constant potential of 1.45 V *vs.* RHE (Figure 3j-k). The characteristic peak at 1697 cm^{-1} is attributed to the C═O stretching vibration of BAD.[51-53] After Ag modification, a new peak gradually intensified over time at 1540 cm^{-1} is observed, which could be attributed to the asymmetric stretching vibration of the -C(O)OH group in BAC.[54] This phenomenon confirms that $Ag/Co(OH)_2$ could further oxidize the Ph-CHO intermediate to BAC.

Density Functional Theory Calculations. In order to deeply investigate the reaction mechanism and C-H bond activation mechanism of AOR over $Ag/Co(OH)_2$, density-functional theory (DFT) calculations were performed. First, $Co(OH)_2$ (100) pure surface as well as Ag-modified $Co(OH)_2$ (100) surface models were constructed for simulating the interfacial effects in the AOR reaction (Figure S25). Density of states (DOS) analysis reveals that compared to pure $Co(OH)_2$, the d-electrons of Co in $Ag/Co(OH)_2$ are more concentrated near the Fermi level, suggesting the higher valence electron density, improved conductivity, and enhanced electron transfer capability (Figure 4a-b).[55,56] Moreover, the d-electron orbitals of Co in $Ag/Co(OH)_2$ exhibit greater dispersion, which means that it has a wider bonding range and the electrons could participate in the reaction more easily. Additionally, the calculated results show that the adsorption energies (E_{ads}) of both BA and BAD on the $Ag/Co(OH)_2$ surface are significantly higher than those on the pure $Co(OH)_2$ surface (Figure 4c, Table S5-S6), and this result is in agreement with

View Article Online
DOI: 10.1039/D5SC09305H

ARTICLE

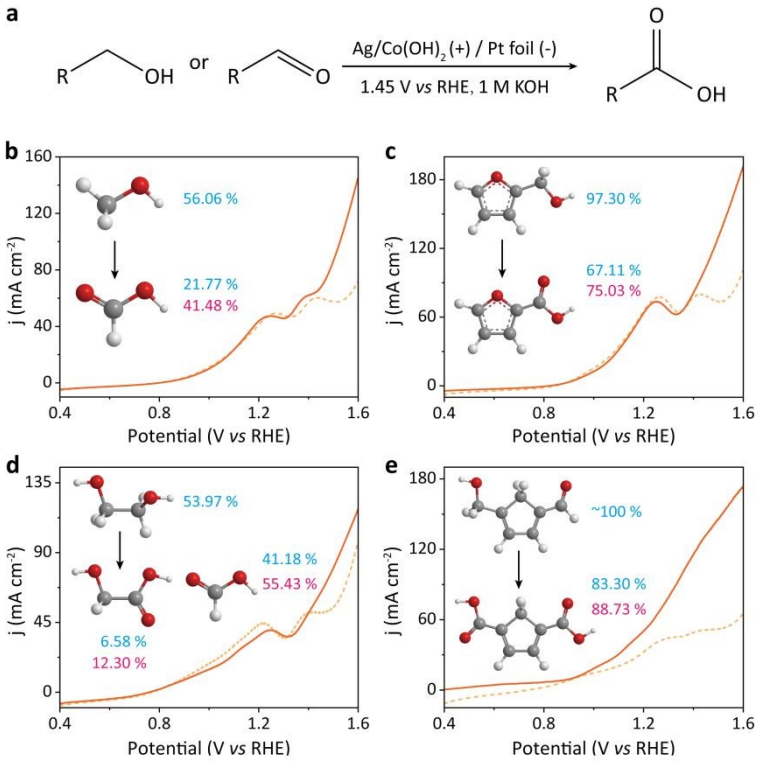

Figure 5. (a) Schematic diagram depicting the pathway for the generation of primary acid at the electrode. (b-e) Electro-oxidative conversion of various substrates into corresponding carboxylic acids catalyzed by $Ag/Co(OH)_2$: (b) MeOH--FA; (c) FFA--FUA; (d) EG--EA and FA; (e) HMF--FDCA. The conversion rate of the substrate and the yield of the acids are indicated in blue font, while the FE of the acids are shown in pink font.

the data from the open circuit potentials and LSV tests (Figure 3a-c). This suggests that $Ag/Co(OH)_2$ has a stronger adsorption affinity for BAD, leading to a lower desorption of BAD, which is more favorable for the subsequent reaction.

In order to gain insight into the effect of the introduction of Ag on the catalyst performance, we investigated in detail the reaction mechanism of the conversion from BA to BAC and the corresponding energy changes. The reaction starts with the co-adsorption of Ph-CH_2OH and OH* on two models, which produces Ph-CHO* after two dehydrogenations. Subsequently Ph-CHO* hydrates in water to form Ph-$CH(OH)_2$*, which then undergoes dehydrogenation to produce Ph-COOH. Throughout the reaction pathway, the potential-determining step (PDS) is the hydration process, which is 1.223 eV and 0.782 eV at the $Co(OH)_2$ and $Ag/Co(OH)_2$ sites, respectively (Figure 4d-e, S26, and Table S7-S8). The introduction of Ag significantly reduces the PDS energy barrier, thus promoting the formation of key intermediates.

Substrate Scope Expansion. Having established that Ag has the ability to enhance the adsorption of Ph-CHO* intermediates and promote highly selective acid production from alcohols, we further demonstrated the oxidative versatility of the catalyst using other monohydric alcohols (methanol (MeOH), furfuryl alcohol (FFA), ethylene glycol (EG), and 5-hydroxymethylfurfuryl aldehyde (HMF)) (Figure 5). The catalytic applicability is initially assessed by LSV, followed by definitive verification of carboxylic acid formation via 1H and 13C nuclear magnetic resonance (NMR) spectroscopy and high-performance liquid chromatography (HPLC) (Figure S27-S30). Notably, no characteristic peaks corresponding to *CHO intermediates were detected, suggesting that potential aldehyde intermediates ware rapidly oxidized under catalytic conditions. Based on the corresponding standard curves (Figure S31-S34), quantitative calculations were performed for the conversion rate of alcohols, the yield of acids, and their purity. The average values obtained from three parallel experiments are marked (Figure 5 and S35), and the standard deviations are listed (Table S9). At 1.45 V *vs.* RHE, $Ag/Co(OH)_2$ exhibits excellent catalytic performance in the oxidation reactions of several alcohols: MeOH conversion reaches 56.06% with formic acid (FA) yield of 21.77% (FE 41.48%); FFA shows 97.30% conversion yielding 67.11% furoic acid (FUA, FE 75.03%); EG achieves 53.97% conversion producing both glycolic acid (GA, yield 6.58%, FE 12.30%) and FA (yield 41.18%, FE 55.43%); while HMF exhibits near-quantitative conversion (~100%) with 2,5-

furandicarboxylic acid yield of 83.30% (FDCA, FE 88.73%). These results show that the designed Ag-modified $Co(OH)_2$ catalysts exhibit excellent versatility in the synthesis of other carboxylic acids.

Conclusions

In summary, we present a highly active and low-cost Ag-modified $Co(OH)_2$ catalyst for the efficient electrocatalytic oxidation of alcohols to carboxylic acids. By enhancing conductivity and forming high-valent Co active sites (Co^{4+}-O), the AOR oxidation current of $Ag/Co(OH)_2$ significantly increases, resulting in the rapid AOR kinetics over a wide potential range and achieving a BAC FE of 99.6 % at 1.45 V *vs.* RHE. The *in-situ* electrochemical experimental results and DFT calculations indicate that Ag modification facilitates electron transfer from alcohols to the catalyst and strengthens the adsorption and activation of key intermediates (Ph-CHO*). The rate-determining step for $Ag/Co(OH)_2$ is the transformation from Ph-CHO* + OH* to Ph-$CH(OH)_2$*, which has an energy barrier of 0.782 eV. This barrier is significantly lower than that on $Co(OH)_2$ (1.223 eV), indicating the high selectivity toward BAC achieved with the $Ag/Co(OH)_2$ catalyst. Furthermore, $Ag/Co(OH)_2$ can also catalyze the conversion of MeOH, FFA, EG and HMF into corresponding carboxylic acids, with FE ranging from 41.48% to 88.73%, demonstrating the universality of the catalyst's strategy for regulating the adsorption energy of intermediates.

Author contributions

Z. Liu and T. Ou Yang conceived and supervised the research, funding acquisition, writing - review & editing. Y. Du conducted the experiments, analyzed the data, and wrote the manuscript. J. Zhang, H. Luo and Y. Zhang assisted with the material synthesis and characterizations. X. Zhang supported supervising and reviewing the manuscript. All authors contributed to the interpretation of the results.

Conflicts of interest

There are no conflicts to declare.

Data availability

All the data supporting this article have been included in the main text and the ESI.†.

Acknowledgements

This work was financially supported by National Natural Science Foundation of China (No. 22379033, U24A20541 and 22278094), Guangdong Basic and Applied Basic Research Foundation (No. 2025B1515020046), Guangzhou Science and Technology Program (No. 2025A03J0011), Basic and Applied Basic Research Pro-gram of Guangzhou (No. SL2024A03J00499), Science and Technology Research Project of Guangzhou (No. 202201020214). We would like to thank Analysis and Test Center of Guangzhou University for their technical support.

Notes and references

1. N. Johnson, M. Liebreich, D. M. Kammen, P. Ekins, R. McKenna and I. Staffell, *Nat. Rev. Clean Technol.*, 2025, **1**, 351-371.
2. S. W. Boettcher, *Chem. Rev.*, 2024, **124**, 13095-13098.
3. X. Zhang, C. Cao, T. Ling, C. Ye, J. Lu and J. Shan, *Adv. Energy Mater.*, 2024, **14**, 2402633.
4. R. Wan, T. Yuan, L. Wang, B. Li, M. Liu and B. Zhao, *Nat. Catal.*, 2024, **7**, 1288-1304.
5. J. Li and H. Duan, *Chem*, 2024, **10**, 3008-3039.
6. X. Huang, O. Akdim, M. Douthwaite, K. Wang, L. Zhao, R. J. Lewis, S. Pattisson, I. T. Daniel, P. J. Miedziak, G. Shaw, D. J. Morgan, S. M. Althahban, T. E. Davies, Q. He, F. Wang, J. Fu, D. Bethell, S. McIntosh, C. J. Kiely and G. J. Hutchings, *Nature*, 2022, **603**, 271-275.
7. Z. Yang, L. Chen, Y. Yin, C. Wei, Z. Xue and T. Mu, *Energy Environ. Sci.*, 2024, **17**, 8801-8809.
8. L. Chen, Z. Yang, Q. Hu, C. Yan, Y. Yao, Y. Bao, Z. Pei, T. Mu and Z. Xue, *Angew. Chem. Int. Ed.*, 2025, **137**, e202511868.
9. J. Zhang, Y. Shen, Z. Wu, X. Zhang, J. Kang, Y. Wu, S. Zhang, S. Chen, G. Wang, H. Zhang, H. Yin and H. Zhao, *Angew. Chem. Int. Ed.*, 2025, **64**, e202423109.
10. Y. Lin, Y. Chen, H. Ren, Y. Sun, J. Chen, M. Wu and Z. Li, *Adv. Funct. Mater.*, 2024, **34**, 2404594.
11. H. Huang, C. Yu, X. Han, H. Huang, Q. Wei, W. Guo, Z. Wang and J. Qiu, *Energy Environ. Sci.*, 2020, **13**, 4990-4999.
12. Z. Wang, J. Li, Q. Zhang, C. Wu, H. Meng, Y. Tang, A. Zou, Y. Zhang, R. Ma, X. Lv, Z. Yu, S. Xi, J. Xue, X. Wang and J. Wu, *Angew. Chem. Int. Ed.*, 2024, **63**, e202411517.
13. S. Li, S. Wang, Y. Wang, J. He, K. Li, J. B. Gerken, S. S. Stahl, X. Zhong and J. Wang, *Nat. Commun.*, 2025, **16**, 266.
14. J. N. Hausmann, P. V. Menezes, G. Vijaykumar, K. Laun, T. Diemant, I. Zebger, T. Jacob, M. Driess and P. W. Menezes, *Adv. Energy Mater.*, 2022, **12**, 2202098.
15. S. Han, L. Sun, D. Fan and B. Liu, *Nat. Commun.*, 2025, **16**, 3426.
16. Y. Yan, J. Zhong, R. Wang, S. Yan and Z. Zou, *J. Am. Chem. Soc.*, 2024, **146**, 4814-4821.
17. L. Wu, Q. Wu, Y. Han, D. Zhang, R. Zhang, N. Song, Y. Fang, H. Liu, M. Wang, J. Chen, A. Du, K. Huang and X. Yao, *J. Am. Chem. Soc.*, 2025, **147**, 18033-18043.
18. Z. Li, Y. Yan, S.-M. Xu, H. Zhou, M. Xu, L. Ma, M. Shao, X. Kong, B. Wang, L. Zheng and H. Duan, *Nat. Commun.*, 2022, **13**, 147.
19. L. Zhang, Y. Liu, L. Li, T. Wu, Q. Wu, J. Z. Y. Seow, X. Lin, S. Sun, L. Tannesia, K. Tang, D. Shao, S. Xi, X. Guo and Z. J. Xu, *Energy Environ. Sci.*, 2025, **18**, 5622-5631.
20. X. Huang, Y. Guo, Y. Zou and J. Jiang, *Appl. Catal, B: Environ.*, 2022, **309**, 121247.
21. C. Jing, T. Yuan, L. Li, J. Li, Z. Qian, J. Zhou, Y. Wang, S. Xi, N. Zhang, H.-J. Lin, C.-T. Chen, Z. Hu, D.-W. Li, L. Zhang and J.-Q. Wang, *ACS Catal.*, 2022, **12**, 10276-10284.

22. K. Xiang, D. Wu, X. Deng, M. Li, S. Chen, P. Hao, X. Guo, J.-L. Luo and X.-Z. Fu, *Adv. Funct. Mater.*, 2020, **30**, 1909610.
23. Y. Q. Zhu, H. Zhou, J. Dong, S. M. Xu, M. Xu, L. Zheng, Q. Xu, L. Ma, Z. Li, M. Shao and H. Duan, *Angew. Chem. Int. Ed.*, 2023, **62**.
24. S. Liu, S. Dou, J. Meng, Y. Liu, Y. Liu and H. Yu, *Appl. Catal, B: Environ.*, 2023, **331**, 122709.
25. Z. He, J. Hwang, Z. Gong, M. Zhou, N. Zhang, X. Kang, J. W. Han and Y. Chen, *Nat. Commun.*, 2022, **13**, 3777.
26. R. Chen, S. Chen, L. Wang and D. Wang, *Adv. Mater.*, 2024, **36**, 2304713.
27. H. Wang, Z. Gao, B. Sun, S. Mu, F. Dang, X. Guo, D. Ma and C. Shi, *Chem Catal.*, 2023, **3**, 100768.
28. S. Liu, J. Lu, X. Yu, H. Pang, Q. Zhang and H. S. Park, *eScience*, 2025, 100378.
29. C. Lee, K. Shin, C. Jung, P.-P. Choi, G. Henkelman and H. M. Lee, *ACS Catal.*, 2020, **10**, 562-569.
30. S. Liu, B. Tian, X. Xu, X. Wang, P. Ran, Y. Sun, J. Wu, A. Qiu, F. Wang, L. Tang, J. Ma and M. Ding, *ACS Catal.*, 2024, **14**, 9476-9486.
31. A.-Z. Li, X. Wang, S. Li, B.-J. Yuan, X. Wang, R.-P. Li, L. Zhang, B.-J. Li and H. Duan, *J. Am. Chem. Soc.*, 2025, **147**, 10493-10503.
32. F. Liu, W. Chen, T. Wang, J. Zhang, D. Yang, Y. Dai, G. Liu, J. Zhou, S. Wang and X. Guan, *Angew. Chem. Int. Ed.*, 2025, **64**, e202415438.
33. X. Lu, Z. Ma, Y. Chang, S. Wang, X. Li, D. Xu, J. Bao and Y. Liu, *Adv. Mater.*, 2024, **36**, 2313057.
34. X. Zhang, L. Hui, F. He and Y. Li, *J. Am. Chem. Soc.*, 2025, **147**, 436-445.
35. A. Moysiadou, S. Lee, C.-S. Hsu, H. M. Chen and X. Hu, *J. Am. Chem. Soc.*, 2020, **142**, 11901-11914.
36. Q. Yan, C. Lian, K. Huang, L. Liang, H. Yu, P. Yin, J. Zhang and M. Xing, *Angew. Chem. Int. Ed.*, 2021, **60**, 17155-17163.
37. S.-L. Xu, W. Wang, Y. Song, R. Tang, Z.-H. Hu, X. Zhou and H.-Q. Yu, *Water Res.*, 2025, **270**, 122851.
38. L. Chen, C. Yu, X. Song, J. Dong, Y. Han, H. Huang, X. Zhu, Y. Xie and J. Qiu, *Small*, 2024, **20**, 2306410.
39. Y. Han, C. Yu, H. Huang, Q. Wei, J. Dong, L. Chen and J. Qiu, *SmartMat*, 2024, **5**, e1206.
40. S. Chongdar, A. Ghosh, R. Bal and A. Bhaumik, *J. Mater. Chem. A*, 2024, **12**, 233-246.
41. L. Ming, X.-Y. Wu, S.-S. Wang, W. Wu and C.-Z. Lu, *Green Chem.*, 2021, **23**, 7825-7830.
42. Y. Zhao, Y. Yan, Y. Wang, E. M. Björk, S. Wang, T. Li, Y. Lu, D. Wang, P. Schaaf, X. Wang and G. Guo, *Mater. Today Energy*, 2025, **48**, 101780.
43. J. Wan, X. Mu, Y. Jin, J. Zhu, Y. Xiong, T. Li and R. Li, *Green Chem.*, 2022, **24**, 4870-4876.
44. L. Wei, M. D. Hossain, M. J. Boyd, J. Aviles-Acosta, M. E. Kreider, A. C. Nielander, M. B. Stevens, T. F. Jaramillo, M. Bajdich and C. Hahn, *ACS Catal.*, 2023, **13**, 4272-4282.
45. J. Zhong, Y. Shen, P. Zhu, S. Yao and C. An, *Nano Res.*, 2023, **16**, 202-208.
46. X. Wen, K. Chen, Y. Su, K. Xiong, P. Fan, J. Wu, C. Liu, Q. Qu and L. Li, *Chem. Eng. J.*, 2024, **493**, 152510.
47. R. Li, P. Kuang, S. Wageh, A. A. Al-Ghamdi, H. Tang and J. Yu, *Chem. Eng. J.*, 2023, **453**, 139797.
48. S. Ye, Z. Chen, G. Zhang, W. Chen, C. Peng, X. Yang, L. Zheng, Y. Li, X. Ren, H. Cao, D. Xue, J. Qiu, Q. Zhang and J. Liu, *Energy Environ. Sci.*, 2022, **15**, 760-770.
49. S. Li, H. Tian, W. Luo, H. Wu, W. Sun, X. Cui and J. Shi, *Small*, 2025, **21**, 2408507.
50. J. Y. Loh, F. M. Yap, T. J. Siang, X. Zeng and W.-J. Ong, *Small*, 2024, **21**, 2409331.
51. Z. Zhang, B.-L. Leng, S.-N. Zhang, D. Xu, Q.-Y. Li, X. Lin, J.-S. Chen and X.-H. Li, *J. Am. Chem. Soc.*, 2024, **146**, 27179-27185.
52. H. Zhang, Y. Gao, S. Meng, Z. Wang, P. Wang, Z. Wang, C. Qiu, S. Chen, B. Weng and Y.-M. Zheng, *Adv. Sci.*, 2024, **11**, 2400099.
53. J. Yu, P. Zhang, L. Li, K. Li, G. Zhang, J. Liu, T. Wang, Z.-J. Zhao and J. Gong, *Nat. Commun.*, 2022, **13**, 7909.
54. R. Liu, W. Tu, A. Pei, W.-H. Huang, Y. Jia, P. Wang, D. Liu, Q. Wu, Q. Qin, W. Zhou, L. Zhou, K. Yan, Y. Zhao and G. Chen, *J. Am. Chem. Soc.*, 2025, **147**, 10339-10348.
55. J. J. Masana, J. Xiao, H. Zhang, X. Lu, M. Qiu and Y. Yu, *Appl. Catal, B: Environ.*, 2023, **323**, 122199.
56. H. Li, K. Gan, R. Li, H. Huang, J. Niu, Z. Chen, J. Zhou, Y. Yu, J. Qiu and X. He, *Adv. Funct. Mater.*, 2023, **33**, 2208622.

View Article Online
DOI: 10.1039/D5SC09305H

View Article Online
DOI: 10.1039/D5SC09305H

Data Availability Statement

The authors confirm that the data supporting the findings of this work are available within the article [and/or] its supplementary materials.